Design and application of the dynamic detection platform for testing the micromechanical properties of agricultural products

Yifeng Hao[1], Yongwei Wang[1,2*], Qianjing Jiang[1], Jing Zhang[1], Jun Wang[1,2]

(1. *Department of Biosystems Engineering, Zhejiang University, Hangzhou 310058, China*;
2. *Key Laboratory of Intelligent Equipment and Robotics for Agriculture of Zhejiang Province, Hangzhou 310058, China*)

Abstract: The micromechanical properties of agricultural products can be used to formulate simulation models and optimize processing parameters for harvest, packaging, and storage. In this study, a detection platform was designed for conducting mechanical tests on different specimens at the tissue level. The system provided controllable and precise displacements; the relative error was less than ±1.0%. The displacement and force measurements were calibrated. Micromechanical tests of apple parenchyma tissues were conducted to evaluate the performance of the proposed platform. The stress-strain curves of the specimens and the micrographs of the microstructures can be obtained simultaneously during the tests. The proposed platform has the capability to test mechanical properties and obtain micro behaviors of agricultural products at the tissue level, which helps in studying the failure mechanism of agricultural products under external loading.

Keywords: elasticity module, micro tensile, parenchyma tissue, micromechanical properties, agricultural products
DOI: 10.25165/j.ijabe.20221506.6548

Citation: Hao Y F, Wang Y W, Jiang Q J, Zhang J, Wang J. Design and application of the dynamic detection platform for testing the micromechanical properties of agricultural products. Int J Agric & Biol Eng, 2022; 15(6): 8–15.

1 Introduction

The mechanical properties of agricultural products are crucial factors for determining their susceptibility to mechanical damage or optimizing the processing parameters during harvest, packaging, storage, and transportation. The macroproperties of agricultural products obtained by universal testing machines are commonly used to establish simulation models for analyzing and predicting their mechanical behaviors[1-5]. These models assume the objects as continuous and homogeneous materials; this makes it difficult to reflect the deformation and failure processes of the microstructures, and to further analyze the conditions in which small injuries occur. Owing to the lack of micromechanical properties, some studies have calibrated their models by adjusting the set values of the micromechanical properties until the macro-parameters match the actual experimental results[6]. However, these input micromechanical parameters may not match the actual properties of the specimens. In other studies, simulation models based on micromechanical properties have helped in analyzing the local failures of objects[7,8]. Some studies have obtained micrographs of microstructures before and after the mechanical damage occurs using electron microscopes, aiming to help explain possible failure mechanisms and the differences in the microproperties of different specimens[9, 10]. However, the observation and detection were not simultaneous, as such the results lacked reliable verification. Thus, it is necessary to detect the micromechanical properties of agricultural products and obtain the deformation of their microstructure simultaneously, to provide the basis for illustrating the mechanical behavior of agricultural products under external loading.

Several methods have been used to determine the micromechanical properties of plants at the tissue level or cell level, including nano-indentation[11-13], and peak-force quantitative nano-mechanical property mapping based on atomic force microscopes[14,15]. These methods provide reliable quantitative results with high resolution, however, require complicated sample preparation. In addition, as the properties are calculated from the static surface properties using mathematical models, it is difficult to detect the anisotropic mechanical properties or deformations at the microstructure level during compression or tensile processes. Thus, a detection device that can conduct micro tensile and compression tests for a specimen, during which the deformation of the microstructure can be identified, is highly desirable.

Some studies have conducted mechanical tests for plant specimens at the cell level or subcellular level and examined their deformations by micromanipulation under microscopes[16-19]. Micro-electro-mechanical-system devices have also been used to test specimens on a small scale[20-22]. However, these systems require complicated and precise operations. Additionally, cells show different mechanical properties when isolated, rather than in tissue[23]. For agricultural use, the deformation and failure processes of specimens at the tissue level are needed. Some studies have combined a micro tensile system with a microscope to detect the micromechanical properties and failure mechanisms, e.g., those of fiber-thermoplastic polymer samples[24] and primary onion epidermal cells[25]. These systems were mainly designed for fibers or thin film samples, and were not available for cuboid specimens and compression tests. Bidhendi et al.[26,27] introduced a simple scalable device for micromechanical tests comprising a linear motorized stage and a stereomicroscope, which could obtain the behaviors of the microstructure during the tests. However, the specimen was fixed on two microscope glass slides; thus, this approach was difficult to apply to cuboid or cylindrical specimens.

Received date: 2021-02-24 **Accepted date:** 2021-12-09
Biographies: Yifeng Hao, MS, research interest: agricultural equipment and robotics, Email: yfhao@zju.edu.cn; **Qianjing Jiang**, PhD, Associate Professor, research interest: agriculture engineering, Email: jqj713@zju.edu.cn; **Jing Zhang**, PhD, research interest: agricultural equipment, Email: 17609004588@163.com; **Jun Wang**, PhD, Professor, research interest: intelligent agricultural equipment, Email: jwang@zju.edu.cn.
***Corresponding author: Yongwei Wang**, PhD, Associate Professor, research interest: planting machinery and fieldwork equipment. No. 866, Yuhang Pond Rood, Xihu District, Hangzhou 310058, China. Tel: +86-18958128068; Fax: +86-571-88982191; Email: wywzju@zju.edu.cn.

Moreover, the deformation of the force sensor needed to be eliminated from the displacement measurements. Alamar et al.[28] studied the effects of storage conditions and cultivars on the micromechanical behaviors of apple tissues. However, only the initial image and that at 80% of the maximal stress were obtained and analyzed. In addition, the sensors of the system could not be easily replaced to measure a wide range of displacements and forces. Liu et al.[29] illustrated the failure behaviors of tomato tissues by manually stretching the specimen using dissecting needles, whilst a proper detection system with controllable displacement is necessary to provide reliable results.

In view of the above, this study aimed to (1) develop a detection platform for the micromechanical properties of different types of agricultural products at the tissue level, by which the deformations of their microstructures could be obtained simultaneously during the entire failure process and to (2) evaluate the detection performance of the proposed system by conducting micromechanical tests, using apple tissue as an example.

2 Materials and methods

2.1 Design of the experimental system

2.1.1 Requirements of the platform

The detection platform is needed to provide the displacement in the tests and to detect the deformation and mechanical load of the specimen with high resolution and accuracy. To fulfill the requirements for the detection of various agricultural products, the designed platform needed to conduct compression tests for cuboid or cylindrical specimens (such as the parenchyma tissues of fruits), and tensile tests for fibers or thin film samples such as peels.

The proposed system consisted of three parts: the hardware system, image acquisition system, and software and control system.

2.1.2 Hardware system

The hardware system (as shown in Figure 1) contained a precision motorized displacement drive module, 3D cartesian coordinate displacement module, linear variable differential transformer (LVDT) distance sensor, force sensor, and several special clamping devices. The precision motorized displacement drive module (MTS25-M-Z8, Thorlabs, USA) was programmable and could provide up to 25 mm linear displacements with a resolution of 29 nm, allowing controllable and micro deformation at the cellular scale.

(1) Arrangement of the force and displacement sensors

The two sensors were attached to the drive module using a designed support, and the force and displacement data were obtained during the tests. The maximum ranges of the force sensor (DYLY-102, DAYSENSOR, China) and LVDT distance sensor (LVDT8-A-10-MM-SL, MIRAN, China) were 10 N and 10 mm, respectively, and the voltage signals from the two sensors were converted to digital signals by a 16-bit A/D module. Force sensors of different ranges could be substituted in the system according to the requirements of the specimens.

(2) Clamping device

Each clamping device could be divided into a movable part and a settled part fixed on the force sensor and 3D Cartesian coordinate displacement module, respectively. Clamping devices with different shapes were designed to meet the requirements of different tests and specimens, as shown in Figure 2. The two parts of the clamping device (Figure 2a) formed a pair of parallel surfaces to fix cuboid or cylindrical specimens, and the specimens were then compressed or extended (after being glued to the device). The top planes of clamping device (Figure 2b) could be used to extend the thin-film samples, whereas clamping device (Figure 2c) could be used for three-point bending tests.

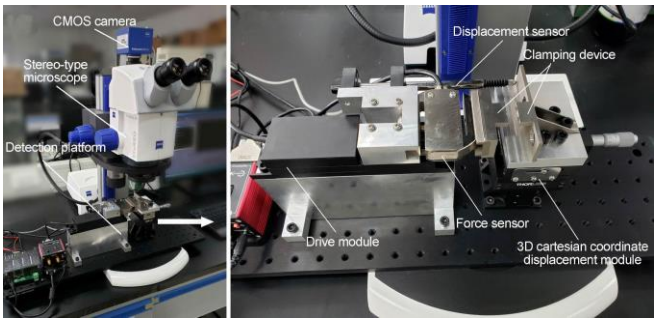

Figure 1 Dynamic detection platform with microstructure visual observation function

a. b. c.

Figure 2 Clamping devices for compression tests (a), tensile tests (b), and three-point bending tests (c)

(3) Manual position adjustment device

The 3D Cartesian coordinate displacement module consisted of a vertical travel stage (MVS005/M, Thorlabs, USA) and two travel translation stages (MT1/M, Thorlabs, USA); these helped to adjust the position of the settled part of the clamping device with a resolution of 10 μm and helped in preloading.

2.1.3 Image acquisition system

A stereomicroscope (SteREO Discovery V8, Zeiss, Germany, with a Max 3.5× objective lens) and a CMOS camera (Axiocam ERc 5s, Zeiss, Germany) were used to obtain the micrographs. The viewing window could be adjusted to obtain images of both the target cell and the whole specimen by changing the objective lens and zoom magnification changer of the microscope body. The stereomicroscope was selected because it met the requirements of dynamic detection. The specimen did not need to be transparent and cut into thin slices, which further allowed for observation of the deformation of the specimen during the compression and tensile tests. In addition, the stereomicroscope had a large working space (i.e., the distance between the objective lens and work platform) for conducting specimen preparations and experimental operation under microscopic observation.

2.1.4 Software and control system

The software of the control system was designed to control the drive module and record and analyze the data from the sensors with the help of a user interface. It was designed to have the following functions.

• Set the parameters of the movement in the tests, including the displacement, moving velocity, and acceleration.

• Collect data from the LVDT distance sensor, force sensor, and camera simultaneously at a set frequency.

• Display the current strain, stress data, and microstructure image in real-time.

• Overload protection.

2.1.5 Mechanical tests workflow with the proposed platform

In the compression test, the specimen was first held near the settled part of the clamping device. The tip of the distance sensor was constantly attached to the settled part during the test. The movable part of the clamping device driven by the drive module moved toward the specimen, and then the 3D Cartesian coordinate displacement module was used to make fine adjustments to ensure

that the specimen was held by the clamping device. As the force sensor responded when the specimen contacted the movable part, the start point of the test was set at that moment. In the tensile test, the distance between the two parts of the clamping device was firstlset to be equal to the length of the specimen. The two ends of the specimen were fixed on the movable part and settled part using glue before the test began.

The stereomicroscope was adjusted to obtain images of the target area. The motion parameters of the drive module, which were determined by the preliminary experiments, were set in the designed control software. When tests began, the force sensor and displacement sensor respectively recorded the stress and deformation of the specimen during the tests as the movable part moved with set parameters. The drive module stopped when it reached maximum displacement. Then the clamping device could be dismantled from the platform and cleared for subsequent tests.

2.2 Platform performance tests

2.2.1 Micrograph measurement

The image scale was first defined before obtaining the microstructural deformations from the micrographs. The micrograph calibration was conducted using an object micrometer and was based on Zen 3.2 microscope software (Zeiss, Germany).

The object micrometer was a glass slide with a standard line of 10 mm in length (Figure 3). The standard line was divided into 100 smaller equal portions, and each portion showed a standard line of 0.1 mm long. The object micrometer was placed under the stereomicroscope, and the lengths of the standard lines shown in the micrographs were measured using the software and compared to the true values.

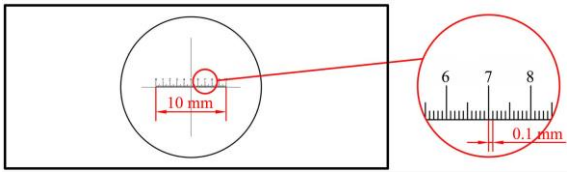

Figure 3 Object micrometer with a 10 mm-long standard line

As shown in Figure 4a, there were six different calibration positions in the viewing window of the stereomicroscope where the object micrometer was placed to show the standard length. For each position, every time the object micrometer was moved slightly different from its original position, and an image was taken to calculate the ratio of the true distance shown by the object micrometer to the distance measured by the software (Figure 4b); this ratio was defined as the dimension calculation factor (f_d). Thus, the length of the object distance in a micrograph could be calculated using Equation (1), as follows:

$$L_o = \frac{N_o}{N_i} \times L_i \times f_d \quad (1)$$

where, L_o was the length of the object distance, mm; L_i was the length of the image scale provided by the Zeiss software, mm; N_o was the number of the pixels of the object distance, and N_i was the number of the pixels of the image scale.

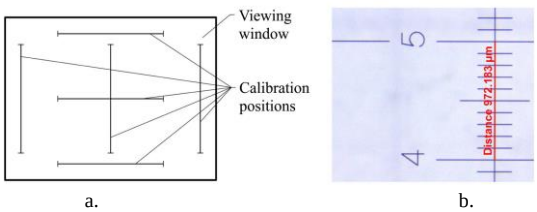

a. b.

Figure 4 Calibration positions (a) and measurement of the right side of the viewing window (b)

2.2.2 Displacement precision and repeatability

After calibrating by the object micrometer, the stereomicroscope was used to evaluate the precision and repeatability of the drive module and displacement sensor. The drive module was set to produce displacements of 1 mm, 3 mm, and 5 mm, respectively, each one for five times. During the movements, the distance measured by the displacement sensor and the stereomicroscope (calibrated by f_d) were compared with the set values of the drive module. The results were used to evaluate whether the drive module produced the required displacement, and to calibrate the measurements of the displacement sensor.

After the drive module and displacement sensor were calibrated, the drive module was set to produce displacements of 1 mm, 2 mm, and 3 mm, respectively, each one for five times. The errors of the drive module and displacement sensor of the final platform were determined.

2.2.3 Deformation measurement

The measurements of the displacement sensor consisted of the deformation of the specimen and the force sensor; the latter needed to be eliminated from the results. The platform was set to conduct compression and tensile tests for the force sensor with no specimen clamped, to obtain the force-displacement curve. The deformation calibration factor (f_p), calculated as the ratio of the deformation of the force sensor to the force, was used to calibrate the detected deformation of the specimens.

2.3 Micromechanical tests

The detection performance of the proposed system was evaluated by conducting micromechanical tests, using apple (*Malus domestica* Borkh.) parenchyma tissue as an example.

2.3.1 Specimen preparation

"Fuji" apples with nearly equal sizes (height: (72.49±2.17) mm, circumference of the middle height: (246.33±3.27) mm and mass (219.92±6.37) g were selected to ensure that all the samples had the same macromechanical properties. Before the tests, all apples were stored in a refrigerator at 4℃ and a relative humidity of 60% for 48 h.

2.3.2 Compression and tensile tests

The tests were designed to obtain the micromechanical properties and failure process of the apple parenchyma tissues and analyze the response of the microstructure to external load. The selected apples were randomly divided into two groups for the compression and tensile tests, respectively. For each group, ten apples were tested. Each specimen taken from the apples was fixed using the clamping device (Figure 5a) and then was compressed or elongated by the designed system. The failure process was recorded using the stereomicroscope. To avoid damage from mechanical clamping, the specimens were glued to the plane of the clamping device with cyanoacrylate[30,31] as an adhesive in the tensile tests. The measured micromechanical properties of the apple parenchyma tissues included the elastic modulus, Poisson's ratio, and yield strength.

2.3.3 Parameters set

To minimize the effects of the cut surface and adhesive on the measurements of the micromechanical properties, the parameters in the test were determined based on several preliminary experiments (data not shown). The different sets of parameters included the length, width, and thickness of the specimen, the manner in which the specimen was glued to the clamping device, and the deformation rate. The results showed that the width of the specimen, the manner in which the specimen was glued to the clamping device, and deformation rate had no significant effect on

the measurements of the elastic modulus of the apple parenchyma tissue, whereas the length and thickness of the specimen significantly affected the measurement results. All of the specimens in the compression and tensile tests were cut to the same size to avoid the effects of their sizes.

Four specimens were taken from each apple at an interval of 90 ° at the median height (Figure 6a); the specimens were obtained from the middle part in the thickness direction of the apple, avoiding being close to the skin and the core (Figure 6b); the arrows show the loading direction for compression tests, whereas the tensile tests were in the opposite direction. A standardized tool with two parallel single-edged blades was used to obtain parenchyma tissue samples of uniform size and shape. The dimensions of the specimens were 5 mm×5 mm×3 mm (shown in Figure 6c), and their actual sizes, which were used to calculate the strain and stress, were measured immediately using the stereomicroscope to avoid water losses. The specimens were stained with 0.1% methylene blue solution for 10 s[32-34] to better show the cell boundaries. In the tensile tests, both ends of the specimen were glued to the clamping device before the tests.

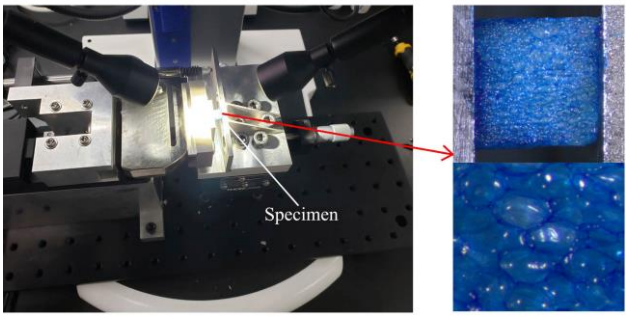

Figure 5 Micromechanical tests based on the detection platform

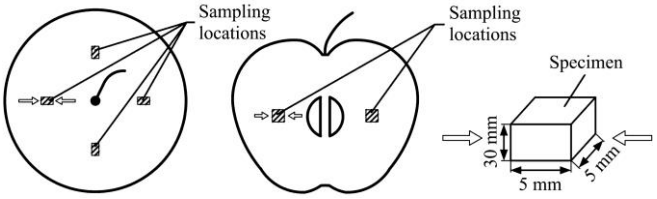

a. b. c.

Figure 6 Sampling locations and the dimensions of specimens

The maximum stress in the compression process of apple tissue occurred when the strain was in the range of 10.2% to 28.3% according to some previous studies[28,35,36]. Thus, the maximum displacement applied to the specimens was set to 2 mm (40% of its original length) to ensure that the maximum stress could be obtained during the tests. The deformation rate was set to 0.6 mm/min for the tests.

2.3.4 Data analysis

(1) Micrograph processing

The images were processed by a specially designed program based on the watershed algorithm, to obtain the responses of different cells, and deformation and damage of the target areas. The watershed algorithm has been widely used in recent studies to separate touching objects, including cell images[37-39].

The primary noise in the micrographs obtained from the camera comprised halation, i.e., the bright areas in the images (Figure 7a), because the stereomicroscope used reflective light to obtain the images. The cell boundaries were not very clear even after staining with methylene blue; therefore, the micrographs were first converted into the HSV color space, as the H channel (Figure 7b) could better display the boundaries while the halation turned to the local minimum area. Then, a median filter was used to remove this halation noise, owing to its good capability in dealing with impulsive noise while preserving edges; after which, there was still some remaining noise. Accordingly, the Sobel operator was used to obtain gradient images in which the remaining noise was the bright area, and a threshold value was used to remove the bright areas. All of the pixels whose values were beyond the threshold value were replaced with the average value of the whole image. Finally, the mark-based watershed algorithm was applied to the gradient images (Figure 7c), and the length of the cell in the loading direction as obtained from the processing program was used to analyze the response of the microstructure. The ratio of deformation in the loading direction to that in the perpendicular direction was calculated to obtain Poisson's ratio.

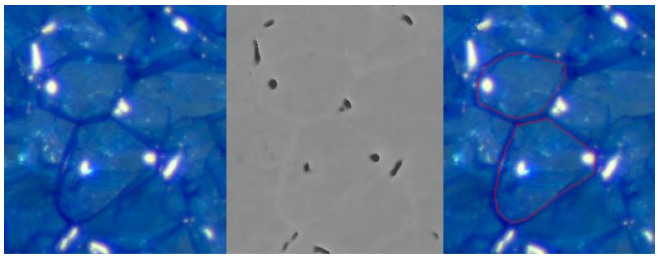

a. b. c.

Figure 7 Original image (a), H channel of the image (b), and the segmentation image (c) of apple parenchyma tissues

(2) Strain and stress calculation

The strains and stresses of the specimens were calculated using the data from the displacement and force sensors. The force sensor showed the force applied to the specimen, and the stress was calculated by the force as combined with the cross-sectional area. The strain was calculated as the ratio of the deformation of the specimen to its initial length. Because the force sensor also had a deformation that was detected by the displacement sensor, the force-displacement curve of the force sensor was initially detected in the platform performance tests to calculate the deformation calibration factor (f_p). Thus, the strain of the specimens was calculated as shown in Equation (2), as follows:

$$\varepsilon_s = (L_d - F_p \times f_p) / L_s \quad (2)$$

where, L_d was the displacement data from the displacement sensor, mm; L_s was the length of the specimen in the loading direction, mm; and F_p was the force data from the force sensor, N.

The stress-strain curves of the specimens and the microstructure images were used to calculate the mechanical properties and analyze the failure processes of tissues.

3 Results and discussion

3.1 Platform calibration and performance

3.1.1 Micrograph measurement calibration

The results of the micrograph calibration are shown in Table 1. There are consistent deviations in all calibration positions (from –2.87% to –2.75%, and the P-value obtained by a one-way analysis of variance is > 0.05), indicating that there is almost no distortion at the edge of the image. Thus, the dimension calculation factor (f_d) is the ratio of the true distance to the measured value, i.e., 1.029.

3.1.2 Displacement precision and repeatability

The measured values from the micrograph (calibrated by f_d) are regarded as the true values, and are compared with the drive module displacement and data from the displacement sensor.

Table 1 Distance measurements in different positions of the viewing area of stereomicroscope

Positions	True distance/μm	Measured value/μm	Standard deviation/μm
Top	1000	971.32 a	0.54
Left side	1000	972.49 a	0.49
Right side	1000	971.57 a	0.48
Bottom	1000	971.22 a	0.99
Horizontal line in the central	1000	971.74 a	0.55
Vertical line in the central	1000	972.10 a	0.44
Average	1000	971.74 a	0.75

Note: Different letters indicate significant differences (p<0.05).

Table 2 Measured values of the distance of drive module displacement from micrograph and displacement sensor (μm)

The set value of drive module	Stereomicroscope			Displacement sensor		
	Measured value	Error[a]	Standard deviation	Measured value	Error[b]	Standard deviation
1000	972.73	+27.27	4.78	1002.56	+29.83	0.23
3000	2978.37	+21.63	5.14	3015.54	+37.17	1.59
5000	4983.34	+16.67	1.46	5031.73	+48.40	3.60

Note: [a] The error was calculated by subtracting the measured value of stereomicroscope from the set value of the drive module. [b] The error was calculated by subtracting the measured value of stereomicroscope from the measured value of the displacement sensor.

The measured values from the micrographs and displacement sensor are listed in Table 2. The errors of the measured displacement of the drive module are positive and do not increase with distance; this is possibly attributed to a mechanical coupling error of the drive module. To calibrate the drive module, the average value of these errors was added to the input value from the designed software, and was subsequently sent to the drive module as the set value in the mechanical tests.

The errors of the data from the displacement sensor are positive, and the standard deviation of the measured value is small. Because the displacement in the micromechanical tests is small (up to 2 mm), the detection errors of the displacement sensor are considered minor and acceptable for this experiment. To simplify the calculation, the displacement sensor was calibrated by subtracting the average value of errors at 1000 μm and 3000 μm from the detection results.

The errors of the final calibrated platform were shown in Table 3. The relative error of the drive module is within ±1.0%, and the relative error of the measurement of the displacement sensor is within ±1.5%.

Table 3 Errors of the drive module and displacement sensor of the final platform

The set value of drive module /μm	Stereomicroscope		Displacement sensor	
	Measured value/μm	Relative error[a]/%	Measured value/μm	Relative error[b]/%
1000	1001.92±10.04	+0.19	1006.46±0.55	+0.45
2000	1983.38±8.18	−0.84	2011.14±0.83	+1.40
3000	2990.38±6.18	−0.32	3015.95±0.96	+0.86

Note: [a] The relative error was calculated as the ratio of the difference between the set value of the drive module and measured value of stereomicroscope to the measured value of stereomicroscope. [b] The relative error was calculated as the ratio of the difference between the measured value of the displacement sensor and measured value of stereomicroscope to the measured value of stereomicroscope.

3.1.3 Deformation measurement calibration

As shown in Figure 8, the relationship between the deformation and force on the force sensor is linear, with R^2 = 0.99. The average value of the deformation calibration factor (f_p) is 9.45×10^{-5} m/N, and the standard deviation is 4.58×10^{-7} m/N. Thus, the deformations of the specimens in the test can be calculated using f_p, based on Equation (2).

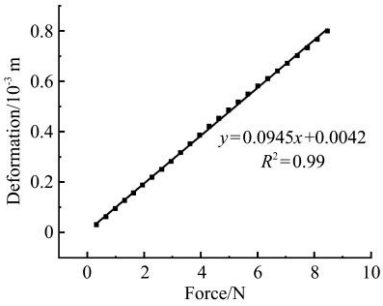

Figure 8 Deformation-force curve of force sensor

3.2 Micromechanical properties

3.2.1 Mechanical properties of apple parenchyma

The stress-strain curve obtained from compression tests (Figure 9a) consists of five stages: an initial stage with a small slope (strain range 0%-4%), a steep linear stage (R^2 = 0.99, strain range 4%-18%), yield stage (strain range 18%-20%), strengthening stage (strain range 20%-25%) and failure stage (strain >25%).

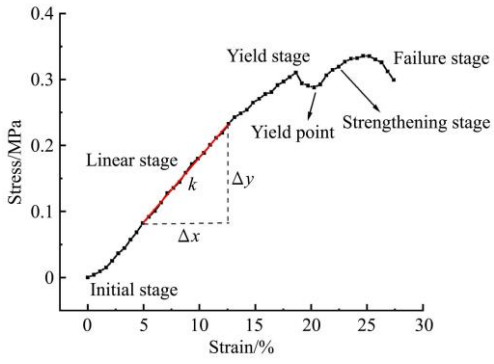

a. Compression

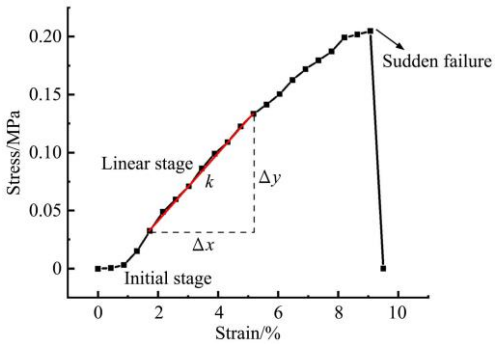

b. Tensile

Figure 9 Stress-strain curves of apple parenchyma in the compression and tensile processes

The elastic modulus of the specimen, i.e., the ratio of the stress to the strain of the specimen, is calculated from the linear stage.

In the tensile tests (Figure 9b), when under a small strain, the stress-strain curve shows the same pattern as in the compression tests. However, the initial stage is much shorter, and the linear stage appears quickly with increasing strain at less than 1% for most specimens. In addition, the yield stage in the tensile process occurs much earlier. Most of the specimens yield under 10% strain, and there is no evident yield point in the stress-strain curve. Thus, the point before specimen failure is taken to calculate the yield strength. A sudden failure occurs when strain reaches 7.49%±1.06%.

The elastic modulus obtained from the tests is shown in Figure 10, and the properties of the apple parenchyma tissues are listed in Table 4.

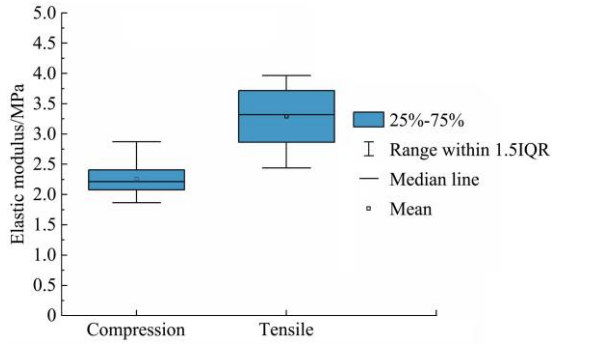

Figure 10 Elastic modulus of apple parenchyma in compression and tensile tests

Table 4 Micromechanical properties of apple parenchyma tissues

Properties	Compression		Tensile	
	Average	Standard deviation	Average	Standard deviation
Elastic modulus/MPa	2.288	0.261	3.265	0.520
Poisson's ratio	0.344	0.031	0.317	0.045
Yield strength/MPa	0.289	0.024	0.193	0.027
Strain at yield point/%[a]	19.45	4.04	7.49	1.06

Note: [a] The yield point in tensile tests were considered as the point just before specimens' failure.

The means of the elastic moduli obtained using the proposed system were similar to those obtained from the same positions by Reference [35] ("Bramley", "Cox", "Norfolk Beefing", and "Rock Pippin"), Reference [36]("Delicious", "Golden Delicious", and "Rome Beauty apples"), Reference [40] ("Golden Delicious"), Reference [28] ("Jonagored" and "Braeburn"), and Reference [41] ("Golden Delicious"). The differences in the elastic modulus can be attributed to the different varieties.

The differences in the mechanical properties from the compression and tensile tests are also shown in Table 4. The elastic modulus of the tissues under tensile loads is greater than that under compression loads. However, the tissues have a larger range of elastic deformation under a compression load, and more easily fail under a tensile load. Some previous studies have also shown different properties from compression and tensile tests of tomato mesocarp tissues[42], potato tissues[43], and apple tissues[28]. A possible explanation is that the mechanisms by which tissues fail are different in compression and tensile processes. The compression failure occurs mainly owing to the rupture of the cell walls caused by the external load, which can be proven by the deformation of the microstructure during the process (Figure 11), whereas the tensile failure mainly occurs owing to the separation of adjacent cells[42]. Vanstreels et al.[44] explained that when onion epidermal tissue was under a tensile load, there was a shear force between the matrix and microfibrils in the cell wall, owing to their different elastic moduli. The fibers slid with respect to each other after reaching the yield point, which was different from the behaviors in the compression process.

3.2.2 Deformation of the microstructure

Compression failure is the main cause of injury to apples during harvest and transportation. As mentioned above, the compression failure process of the apple parenchyma tissue can be divided into several stages. The deformations of microstructures during the tests were obtained by the proposed system (Figure 11), which also showed different patterns in each stage. The compression failure behaviors of the apple parenchyma tissues could be further illustrated based on the stress-strain curves and deformations of the microstructures.

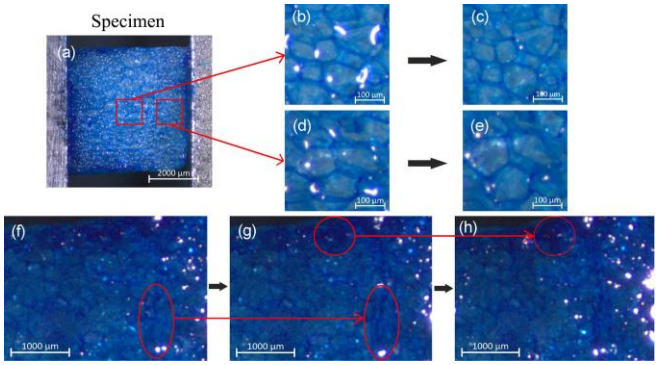

a. Initial condition from the micrograph b. Initial condition of the cells at the central part c. The cells at the central part when the strain of whole tissues reached 8.77% d. Initial condition of the cells near the clamping device e. The cells near the clamping device when the strain of whole tissues reached 8.77% f. No local failure g. Local failure started to occur h. Multiple local failures occurred

Figure 11 Compression failure process of the apple parenchyma tissue

(1) Initial stage

When the tissues were under a small strain, there was no significant deformation of the cells in this stage. As the strain increased, the deformation of the cells became visible. This initial stage was also found by Alamar et al.[28], which was owing to the compression of the intercellular spaces in the tissue. Jarvis et al.[45] reported that these intercellular spaces can be filled with air for gas transportation or water, and they occupy a large fraction of the tissues. Some studies have considered the intercellular spaces in the microstructure model of fruits[46,47]. Changes in the intercellular spaces in apple tissue were observed during glucose and sucrose osmotic dehydration[48]. The intercellular spaces were the ones that first responded to the external load and began to deform, which also contributed to the initial stage shown in the stress-strain curves.

(2) Linear stage

As the stress continued to increase, the strain of the tissue increased linearly with the stress. However, the deformations of different parts of the tissue were not synchronous at this stage. The cells near the clamping device began to deform first and even failed (Figures 11d and 11e), whereas the volume of cells located in the central part of the tissues did not change even the strain of the whole tissues reached nearly 10% (Figures 11b and 11c). The deformation of the parenchyma tissues was mainly provided by the parts near the external load.

(3) Maximum stress before yield

With the micrographs of the microstructure, it can be found that before the strengthening stage, the stress reached the maximum value just before local failure began to occur in the tissue (Figure 11g). The volume of the broken cells in those parts decreased rapidly with the outflow of the cell sap, whereas the other parts remained intact. According to the report of Cardenas-Perez et al.[23], there are large differences in the Young's moduli among different apple cells (0.86 MPa±0.81 MPa). In this study, as the stress increased, some cells in the tissue reached their limit and broke first, leading to a decrease in stress. Therefore, irreversible damage to the microstructure occurred at this time and would develop into bruising or decayed areas.

(4) Yield stage

After entering the yield stage, with the increasing stain, other local failures occurred in different areas of the tissue (Figure 11h).

4 Conclusions

In this study, a detection platform was designed for studying the micromechanical properties of agricultural products. Special clamping devices were designed to conduct compression, tensile and three-point bending tests for specimens at the tissue level. The system provided controllable and precise displacements; the relative error was less than ±1.0%. The displacement measurements were calibrated, and the deformation of the force sensor was eliminated from the displacement measurements. The microstructure of the specimen could be obtained using a stereomicroscope during the tests.

The performance of the proposed platform was evaluated by conducting micromechanical tests of apple parenchyma tissues. The stress-strain curves, as well as the micrographs of the microstructures of the specimens can be obtained simultaneously. The detection results demonstrated the capability of this platform to detect the micromechanical properties of plant tissues with high resolution, and to provide the deformations of the microstructures for further analysis of the failure process of plant tissues.

In summary, the proposed platform has the capability to detect the mechanical properties of agricultural products at the tissue level, and to simultaneously obtain the deformations of their microstructures, which help in studying failure mechanisms of plant tissues in the future.

Acknowledgements

The authors would like to thank the National Natural Science Foundation of China for the financial support of the project “Study on kinematics and dynamics of pollen and pneumatic pollination method in hybrid rice seed production” (Grant No. 31971796). The research was also supported by the Earmarked Fund of CARS-01.

[References]

[1] Ahmadi E, Barikloo H, Kashfi M. Viscoelastic finite element analysis of the dynamic behavior of apple under impact loading with regard to its different layers. Comput Electron Agric, 2016; 121: 1–11.

[2] Carvalho E D, Magalhaes R R, Santos F L. Geometric modeling of a coffee plant for displacements prediction. Comput Electron Agric, 2016; 123: 57–63.

[3] Du D D, Wang B, Wang J, Yao F Q, Hong X Z. Prediction of bruise susceptibility of harvested kiwifruit (*Actinidia chinensis*) using finite element method. Postharvest Biol Technol, 2019; 152: 36–44.

[4] Edrris M K, Al-Gaadi K A, Hassaballa A A, Tola E, Ahmed K A M. Impact of soil compaction on the engineering properties of potato tubers. Int J Agric Biol Eng, 2020; 13(2): 163–167.

[5] Zhang B H, Guan S J, Ning X F, Gong Y J. Mechanical characteristics of Hanfu apple at low temperature. Int J Agric Biol Eng, 2014; 7(3): 107–113.

[6] Sadrmanesh V, Chen Y. Simulation of tensile behavior of plant fibers using the discrete element method (DEM). Composites Part a-Applied Science and Manufacturing, 2018; 114: 196–203.

[7] Li Z G, Andrews J, Wang Y Q. Mathematical modelling of mechanical damage to tomato fruits. Postharvest Biol Technol, 2017; 126: 50–56.

[8] Diels E, Wang Z, Nicolai B, Ramon H, Smeets B. Discrete element modelling of tomato tissue deformation and failure at the cellular scale. Soft Matter, 2019; 15(16): 3362–3378.

[9] Bargel H, Neinhuis C. Tomato (*Lycopersicon esculentum* Mill.) fruit growth and ripening as related to the biomechanical properties of fruit skin and isolated cuticle. J Exp Bot, 2005; 56(413): 1049–1060.

[10] Nikara S, Ahmadi E, Nia A A. Finite element simulation of the micromechanical changes of the tissue and cells of potato response to impact test during storage by scanning electron microscopy. Postharvest Biol Technol, 2020; 164: 111153. doi: 10.1016/j.postharvbio.2020.111153.

[11] Jakes J E, Frihart C R, Beecher J F, Moon R J, Stone D S. Experimental method to account for structural compliance in nanoindentation measurements. J Mater Res, 2008; 23(4): 1113–1127.

[12] Meng Y J, Wang S Q, Cai Z Y, Young T M, Du G B, Li Y J. A novel sample preparation method to avoid influence of embedding medium during nano-indentation. Applied Physics a-Materials Science & Processing, 2013; 110(2): 361–369.

[13] Zhou X W, Ren S H, Lu M Z, Zhao S T, Chen Z J, Zhao R J, et al. Preliminary study of cell wall structure and its mechanical properties of C3H and HCT RNAi transgenic poplar sapling. Sci Rep, 2018; 8: 10508. doi: 10.1038/s41598-018-28675-5.

[14] Arnould O, Siniscalco D, Bourmaud A, Le Duigou A, Baley C. Better insight into the nano-mechanical properties of flax fibre cell walls. Ind Crops Prod, 2017; 97: 224–228.

[15] Siniscalco D, Arnould O, Bourmaud A, Le Duigou A, Baley C. Monitoring temperature effects on flax cell-wall mechanical properties within a composite material using AFM. Polym Test, 2018; 69: 91–99.

[16] Shiu C, Zhang Z, Thomas C R. A novel technique for the study of bacterial cell mechanical properties. Biotechnol Tech, 1999; 13(10): 707–713.

[17] Blewett J, Burrows K, Thomas C. A micromanipulation method to measure the mechanical properties of single tomato suspension cells. Biotechnol Lett, 2000; 22(23): 1877–1883.

[18] Thomas C R, Zhang Z, Cowen C. Micromanipulation measurements of biological materials. Biotechnol Lett, 2000; 22(7): 531–537.

[19] Wang L, Hukin D, Pritchard J, Thomas C. Comparison of plant cell turgor pressure measurement by pressure probe and micromanipulation. Biotechnol Lett, 2006; 28(15): 1147–1150.

[20] Liu R, Wang H, Li X P, Ding G F, Yang C S. A micro-tensile method for measuring mechanical properties of MEMS materials. J Micromech Microeng, 2008; 18(6): 065002. doi: 10.1088/0960-1317/18/6/065002.

[21] Torrents A, Azgin K, Godfrey S W, Topalli E S, Akin T, Valdevit L. MEMS resonant load cells for micro-mechanical test frames: feasibility study and optimal design. J Micromech Microeng, 2010; 20(12): 125004. doi: 10.1088/0960-1317/20/12/125004.

[22] Zamil M S, Yi H J, Haque M A, Puri V M. Characterizing microscale biological samples under tensile loading: stress-strain behavior of cell wall fragment of onion outer epidermis. American Journal of Botany, 2013; 100(6): 1105–1115.

[23] Cardenas-Perez S, Chanona-Perez J J, Mendez-Mendez J V, Calderon-Dominguez G, Lopez-Santiago R, Arzate-Vazquez I. Nanoindentation study on apple tissue and isolated cells by atomic force microscopy, image and fractal analysis. Innovative Food Sci Emerg Technol, 2016; 34: 234–242.

[24] Yang L, Thomason J L. Development and application of micromechanical techniques for characterising interfacial shear strength in fibre-thermoplastic composites. Polym Test, 2012; 31(7): 895–903.

[25] Zamil M S, Yi H J, Puri V M. The mechanical properties of plant cell walls soft material at the subcellular scale: the implications of water and of the intercellular boundaries. J Mater Sci, 2015; 50(20): 6608–6623.

[26] Bidhendi A J, Li H B, Geitmann A. Modeling the nonlinear elastic behavior of plant epidermis. Botany, 2020; 98(1): 49–64.

[27] Bidhendi A J, Zamil M S, Geitmann A. Assembly of a simple scalable device for micromechanical testing of plant tissues. Methods in Cell Biology, 2020; 160: 327–348.

[28] Alamar M C, Vanstreels E, Oey M L, Molto E, Nicolai B M. Micromechanical behaviour of apple tissue in tensile and compression tests: Storage conditions and cultivar effect. J Food Eng, 2008; 86(3): 324–333.

[29] Liu Z G, Li Z G, Yue T L, Diels E, Yang Y G. Differences in the cell morphology and microfracture behaviour of tomato fruit (*Solanum lycopersicum* L.) tissues during ripening. Postharvest Biol Technol, 2020; 164: 111182. doi: 10.1016/j.postharvbio.2020.111182.

[30] Pitts M J, Davis D C, Cavalieri R P. Three-point bending: An alternative method to measure tensile properties in fruit and vegetables. Postharvest Biol Technol, 2008; 48(1): 63–69.

[31] Bruggenwirth M, Knoche M. Cell wall swelling, fracture mode, and the mechanical properties of cherry fruit skins are closely related. Planta, 2017; 245(4): 765–777.

[32] Sterling C. Effect of low temperature on structure and firmness of apple tissue. J Food Sci, 1968; 33(6): 577–580.

[33] Lewicki P P, Porzecka-Pawlak R. Effect of osmotic dewatering on apple

tissue structure. J Food Eng, 2005; 66(1): 43–50.
[34] Mayor L, Silva M A, Sereno A M. Microstructural changes during drying of apple slices. Drying Technol, 2005; 23(9-11): 2261–2276.
[35] Khan A A, Vincent J F V. Compressive stiffness and fracture properties of apple and potato parenchyma. J Texture Stud, 1993; 24(4): 423–435.
[36] Abbott J A, Lu R. Anisotropic mechanical properties of apples. Transactions of the Asae, 1996; 39(4): 1451–1459.
[37] Liu M, Chakraborty A, Singh D, Yadav R K, Meenakshisundaram G, Reddy G V, et al. Adaptive cell segmentation and tracking for volumetric confocal microscopy images of a developing plant meristem. Molecular Plant, 2011; 4(5): 922–931.
[38] Marcuzzo M, Quelhas P, Campilho A, Mendonca A M, Campilho A. Automated Arabidopsis plant root cell segmentation based on SVM classification and region merging. Comput Biol Med, 2009; 39(9): 785–793.
[39] Chau Z H, Paranawithana I, Yang L, Tan U, editors. Plant cell segmentation with adaptive thresholding. In Proceedings of the 25th International Conference on Mechatronics and Machine Vision in Practice (M2VIP), Stuttgart-Germany, 2018; pp.108–113.
[40] Grotte M, Duprat F, Pietri E, Loonis D. Young's modulus, Poisson's ratio, and Lame's coefficients of Golden Delicious apple. Int J Food Prop, 2002; 5(2): 333–349.
[41] Shirvani M, Ghanbarian D, Ghasemi-Varnamkhasti M. Measurement and evaluation of the apparent modulus of elasticity of apple based on Hooke's, Hertz's and Boussinesq's theories. Measurement, 2014; 54: 133–139.
[42] Li Z G, Li P P, Yang H L, Liu J Z, Xu Y F. Mechanical properties of tomato exocarp, mesocarp and locular gel tissues. J Food Eng, 2012; 111(1): 82–91.
[43] Scanlon M G, Long A E. Fracture strengths of potato tissue under compression and tension at 2 rates of loading. Food Res Int, 1995; 28(4): 397–402.
[44] Vanstreels E, Alamar A C, Verlinden B E, Enninghorst A, Loodts J K A, Tijskens E, et al. Micromechanical behaviour of onion epidermal tissue. Postharvest Biol Technol, 2005; 37(2): 163–173.
[45] Jarvis M C, Briggs S P H, Knox J P. Intercellular adhesion and cell separation in plants. Plant Cell and Environment, 2003; 26(7): 977–989.
[46] Ho Q T, Verboven P, Verlinden B E, Lammertyn J, Vandewalle S, Nicolai B M. A continuum model for metabolic gas exchange in pear fruit. PLoS Comput Biol, 2008; 4(3): e1000023. doi: 10.1371/journal.pcbi.1000023.
[47] Rahman M M, Gu Y T, Karim M A. Development of realistic food microstructure considering the structural heterogeneity of cells and intercellular space. Food Structure-Netherlands, 2018; 15: 9–16.
[48] Nieto A B, Salvatori D M, Castro M A, Alzamora S M. Structural changes in apple tissue during glucose and sucrose osmotic dehydration: shrinkage, porosity, density and microscopic features. J Food Eng, 2004; 61(2): 269–278.